

# The BOOMERANG North America instrument: a balloon-borne bolometric radiometer optimized for measurements of cosmic background radiation anisotropies from $0.3^\circ$ to $4^\circ$ .

F. Piacentini<sup>1</sup>, P.A.R. Ade<sup>2</sup>, R. Bathia<sup>3</sup>, J.J. Bock<sup>3,4</sup>, A. Boscaleri<sup>5</sup>, P. Cardoni<sup>6</sup>, B.P. Crill<sup>3</sup>, P. de Bernardis<sup>1</sup>, H. Del Castillo<sup>4</sup>, G. De Troia<sup>1</sup>, P. Farese<sup>1</sup>, M. Giacometti<sup>1</sup>, E.F. Hivon<sup>3</sup>, V.V. Hristov<sup>3</sup>, A. Iacoangeli<sup>1</sup>, A.E. Lange<sup>3</sup>, S. Masi<sup>1</sup>, P.D. Mauskopf<sup>3,7</sup>, L. Miglio<sup>1,8</sup>, C.B. Netterfield<sup>3,8</sup>, P. Palangio<sup>9</sup>, E. Pascale<sup>3,5</sup>, A. Raccanelli<sup>1</sup>, S. Rao<sup>1,9</sup>, G. Romeo<sup>9</sup>, J. Ruhl<sup>10</sup>, F. Scaramuzzi<sup>6</sup>

## ABSTRACT

We describe the BOOMERANG North America (BNA) instrument, a balloon-borne bolometric radiometer designed to map the Cosmic Microwave Background (CMB) radiation with  $0.3^\circ$  resolution over a significant portion of the sky. This receiver employs new technologies in bolometers, readout electronics, millimeter-wave optics and filters, cryogenics, scan and attitude reconstruction. All these subsystems are described in detail in this paper. The system has been fully calibrated in flight using a variety of techniques which are described and compared. Using this system, we have obtained a measurement of the first peak in the CMB angular power spectrum in a single, few hour long balloon flight. The instrument described here was a prototype of the BOOMERANG Long Duration Balloon (BLDB) experiment.

---

<sup>1</sup>Dipartimento di Fisica, Universita' La Sapienza, P.le A. Moro 2, 00185, Roma, Italy, e-mail: francesco.piacentini@roma1.infn.it

<sup>2</sup>Department of Physics, Queen Mary and Westfield College, Mile End Road, London, E1 4NS, U.K.

<sup>3</sup>Department of Physics, Math, and Astronomy, California Institute of Technology, Pasadena, CA, USA

<sup>4</sup>Jet Propulsion Lab, Pasadena, CA, USA

<sup>5</sup>IROE-CNR, Via Panciatichi 54, 50127 Firenze, Italy

<sup>6</sup>Ente Nazionale Energie Alternative, Frascati, Italy

<sup>7</sup>Dept. of Physics and Astronomy, University of Massachusetts, Amherst, MA, USA

<sup>8</sup>Department of Astronomy, University of Toronto, Canada

<sup>9</sup>Istituto Nazionale di Geofisica, Roma, Italy

<sup>10</sup>Dept. of Physics, Univ. of California, Santa Barbara, CA, USA

*Subject headings:* cosmology: observations — cosmic microwave background — instrumentation: photometers

## 1. Introduction

The existence of the 2.7 K Cosmic Microwave Background (CMB) Radiation is evidence that our universe originated from a hot, dense plasma (Hu *et al.* 1997). This radiation was emitted in the early universe, when the plasma cooled enough for protons and electrons to form hydrogen atoms. Before recombination, photons and baryons were tightly coupled by Compton scattering. After recombination the photons and baryons are highly decoupled, with a mean free path longer than the causal horizon. This event is dated  $\sim 300000$  years after the Big Bang when the universe was  $\sim 1000$  times smaller and  $\sim 50000$  times younger (red shift  $z=1000$ ). The properties of the CMB reflect the conditions of the early universe and are closely linked with global properties of the universe, such as the energy density ( $\Omega_{tot}$ ), composition ( $\Omega_b$ ,  $\Omega_\Lambda$ ,  $\Omega_{DM}$ ), and expansion rate ( $H_0$ ).

In particular, variations in the brightness of the CMB, or anisotropies, reflect variations in temperature, density, and velocity of the last scattering surface. These fluctuations, that originated from random noise at an earlier phase of expansion, are the seeds for the formation of structures such as galaxies and clusters of galaxies present in the universe today. Precise measurements of the angular power spectrum of CMB anisotropies (White *et al.* 1994) will discriminate between competing cosmological models and, if the inflationary scenario is correct, will accurately determine many of the physical parameters of the universe.

The COBE-DMR detection (Smoot *et al.* 1991; Smoot *et al.* 1992) of anisotropies in the CMB at large angular scales provides a point of reference for theoretical models of the origin of fluctuations in the CMB (Bond *et al.* 1994). Measurements at smaller angular scales are needed to fully understand the nature of these fluctuations. Since the launching of COBE, many other experiments have made significant detections of CMB anisotropy at a wide variety of angular scales, from  $0.3^\circ$  to  $10^\circ$ , but until 1998, none of the measurements provided enough information for serious cosmological parameter determination.

The new generation of CMB experiments is designed to probe models of structure formation with a combination of higher sensitivity, sky coverage and resolving power. Advances in detector technology have resulted in radiometers that are over 100 times more sensitive than the COBE-DMR per unit time. In addition, improved techniques for removing noise from atmospheric fluctuations with both single dish instruments and interferometers allow increased sensitivity with ground-based telescopes. Long Duration Balloon (LDB) platforms

provide the opportunity to obtain the long integration times needed for large sky coverage with balloon-borne telescopes.

BOOMERANG is an experiment designed to measure the detailed structure of the CMB at angular scales from  $0.2^\circ$  to  $4^\circ$  with high sensitivity. The BOOMERANG instrument consists of a 1.3 m balloon-borne telescope and pointing platform with a 300 mK bolometric array receiver. The receiver is contained inside a liquid Nitrogen (LN2) and liquid Helium (LHe) cryostat with a hold-time of two weeks.

The measurement technique consists of measuring a sky brightness map by slowly scanning the telescope (and the full payload) in azimuth, using the earth rotation to cover a wide sky region. There is no mechanical chopper. The scan converts CMB anisotropies at different angular scales into detector signals at different sub-audio frequencies. The instrument features a new total power readout of the detectors, optimized to preserve the information content of the signal while rejecting very low and very high frequency noise. This approach pioneers in several aspects the HFI instrument on the Planck satellite.

In this paper we describe the instrument prototype as it was used for the test flight, on Aug.30, 1997, to qualify all the flight subsystems for later use in the Antarctic LDB flight. During the 1997 test flight we observed about 200 square degrees of sky at high Galactic latitudes. Science results from that flight are reported in (Mauskopf *et al.* 2000) and (Melchiorri A. *et al.* 2000). Here we give all the technical details of the instrument as well as its performance during the test flight: thermal performance, bolometer loading and noise, scan performance, attitude reconstruction, calibration on Jupiter and on the CMB Dipole. The LDB instrument is described in (Crill *et al.* 2001).

## 2. Instrument

BOOMERANG is designed to take advantage of the long integration time possible from a balloon borne platform flown over the Antarctic. Antarctic summer ballooning is very attractive for CMB anisotropy experiments for two reasons. The first is that the flight duration (up to  $\sim 20$  days) allows for substantial sky coverage and deep checks for systematics; the second is that very low foreground regions are observable in the direction generally opposite the sun during the Antarctic summer.

There are, however, a number of challenges peculiar to Antarctic ballooning. The long flight duration requires special cryogenic systems. The cosmic ray flux in polar regions is enhanced by a factor of about ten with respect to North American latitudes, thus resulting in a high noise in standard bolometric detectors. The continual presence of the sun during

an Antarctic LDB flight is a general concern for the thermal performance of the payload and for pickup in the sidelobes of the telescope. The balloon is far from the ground equipment, so special data collection and telemetry systems have to be used, and interactivity with the system is reduced.

We describe in the following the solutions we have adopted to overcome these problems, developing custom subsystems: a long duration cryostat, spider-web bolometers, low sidelobes off-axis optics, special sun shields and telescope baffling, total power readout.

A general view of the experiment with its main subsystems is shown in Figure 1.

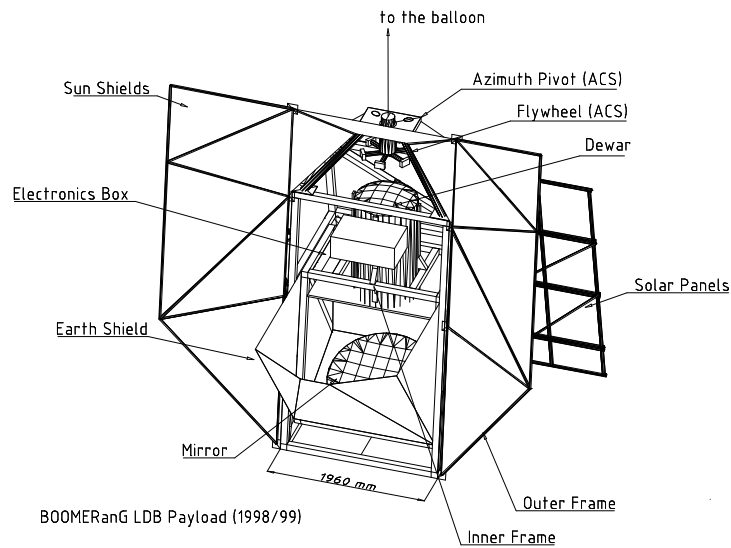


Fig. 1.— BOOMERANG payload. Special shields in aluminized mylar protect from sun and earth radiation reducing sidelobes. Radiation coming from the sky is reflected into the cryostat by means of the 1.3 m primary mirror. Solar panel are used for power supply in the LDB flight while Lithium batteries were used in the BNA flight. The Attitude Control System (ACS) provides pointing and scanning of the telescope.

## 2.1. Optics

The BOOMERANG telescope consists of an ambient temperature 1.3 m diameter off-axis parabolic primary mirror ( $f=1280$  mm,  $45^\circ$  off-axis) which feeds cold reimaging secondary and tertiary mirrors inside a large liquid helium cryostat. The telescope and the cryostat are both mounted on an aluminum frame (the inner frame of the payload) which can be tipped in elevation by  $-12^\circ$  to  $+20^\circ$  to cover elevation angles from  $33^\circ$  to  $65^\circ$ . The primary mirror has a  $45^\circ$  off-axis angle. Radiation from the sky is reflected by the primary mirror and enters the cryostat through a thin ( $50 \mu\text{m}$ ) polypropylene window near the prime focus. Two circular windows side by side, each 66 mm in diameter, are used. This geometry provides a wide field of view while allowing the use of thin window material which minimizes the emission from this ambient temperature surface. Filters rejecting high frequency radiation are mounted on the 77 K and 2 K shields in front of the cold reimaging optics. Fast off-axis secondary and tertiary mirrors surrounded by absorbing baffles reimagine the prime focus onto the detector focal plane.

The BOOMERANG optics (Figure 2) is optimized for an array with widely separated pixels. The advantage of having large spacing between pixels in the focal plane is the ability to difference (or compare) the signals from two such pixels and remove correlated optical fluctuations such as temperature drift of the telescope, while retaining high sensitivity to structure on the sky at angles up to the pixel separation. This scheme eliminates the need for moving optical components and simplifies the design and operation of the experiment.

We optimized the optics for diffraction limited performance at 1 mm over a  $2^\circ \times 5^\circ$  field of view. The reimaging optics are configured to form an image of the primary mirror at the 10 cm diameter tertiary mirror. The size of the tertiary mirror therefore limits the illumination pattern on the primary mirror, which is underfilled by 50% in area (85 cm in diameter) to improve sidelobe rejection.

The secondary mirror is an ellipsoid and the tertiary is a paraboloid, 10 cm in diameter, corresponding to an 85 cm diameter aperture on the 1.3 m primary mirror. The equation describing the three mirrors is

$$z(r) = \frac{r^2}{R \left[ 1 + \sqrt{1 - (1+k)\frac{r^2}{R^2}} \right]} + Ar^4 + Br^6 \quad (1)$$

with parameters  $R$ ,  $k$ ,  $A$ ,  $B$  as in Table 1.

The BNA focal plane contains single frequency channels fed by conical or Winston horns. Although the image quality from the optics is diffraction limited over a  $2^\circ \times 5^\circ$  field, all of the feed optics are placed inside two circles  $2^\circ$  in diameter, separated by  $3.5^\circ$  center

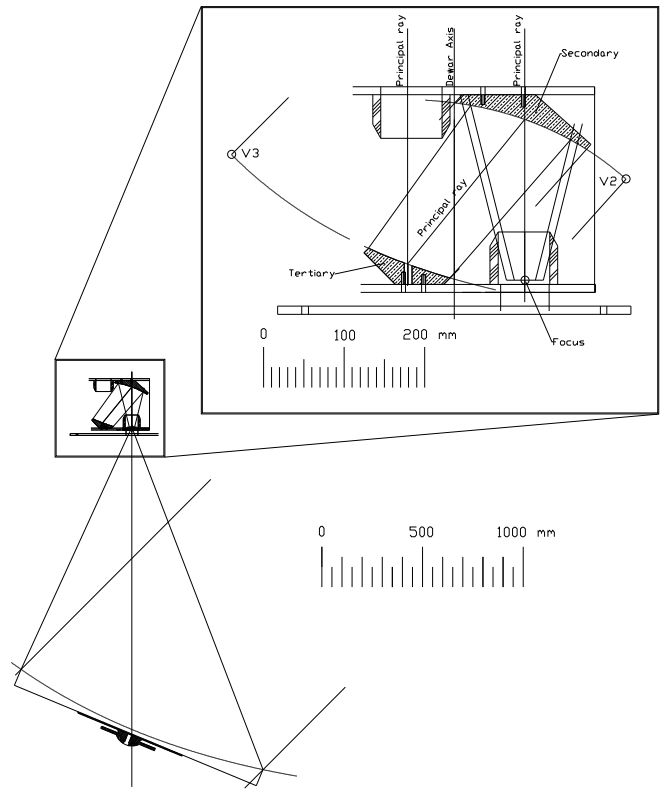


Fig. 2.— BOOMERANG optics. Secondary and tertiary mirrors project the image on the focal plane. They are cooled to 2 K inside the main cryostat. An image of the 1.3 m primary mirror is formed on the tertiary mirror which works as a cold Lyot stop, improving the off-axis rejection of the photometer.

to center. The focal plane area outside these circles is vignetted by blocking filters at the entrance to the optics box and on the 77 K shield and is unusable. Due to the curvature of the focal plane, the horns are placed at the positions of the beam centroids determined by geometric ray tracing. All of the feeds are oriented towards the center of the tertiary mirror. The configuration of the focal plane for the North American Flight is in Figure 3.

The BNA frequency bands are centered at 90 and 150 GHz and are optimized to maximize sensitivity to CMB fluctuations, identify dust emission and reject radiation from atmospheric line emission. The low pass filters mounted on the 77 K and 2 K optical entrance windows provide good transmission across these bands while effectively blocking higher frequency radiation. Two metal mesh low pass filters with cutoff frequencies of 480 GHz are mounted on the 77 K stage. The filters are 65 mm in diameter and each one is directly

Mirror	$R$ (mm)	$k$	$A$ (mm <sup>-3</sup> )	$B$ (mm <sup>-5</sup> )
Primary	2560	-1.0	0.0	0.0
Secondary	363.83041	-0.882787413818	$1.3641139 \times 10^{-9}$	$1.8691461 \times 10^{-15}$
Tertiary	545.745477407	-1.0	$4.3908607 \times 10^{-10}$	$-3.2605391 \times 10^{-15}$

Table 1: Ideal parameters for the equation of the three BOOMERANG mirrors (see eqn.1)

behind one of the 50  $\mu\text{m}$  polypropylene vacuum windows. Two more low pass filters with a cutoff frequency of 300 GHz are mounted on the 2 K stage at the entrance to the cold optics box. Although each filter has a leak at twice the cutoff frequency, the combination eliminates these leaks. Because these filters are reflective at frequencies above the cutoff, they minimize the radiation heat load on the cryogenics. While the metal mesh filters have high reflectivity at high frequencies, they are not impenetrable, and above a few THz any transmission at the level of less than  $10^{-3}$  is significant. Therefore, we place a dielectric absorber behind the 300 GHz filter on the 2 K stage that has a cutoff frequency of 1650 GHz. The absorber is 0.5 mm thick alkali-halide filter coated with a 130  $\mu\text{m}$  thick layer of black polyethylene. This low pass filter stack has a transmission of  $> 80\%$  at all frequencies from 90 to 410 GHz, while attenuates by a factor  $5 \cdot 10^{-4}$  between 1650 GHz and 100 THz and by a factor  $10^{-3}$  over 100 THz. All of the other filtering is done in the focal plane elements.

We have produced two different feeds designed to efficiently couple to the telescope and produce beam sizes on the sky of 20' and 40'. These sizes are larger than the diffraction limit: we traded resolution for throughput to obtain good sensitivity to diffuse radiation even in a short test flight. The design of the single frequency feed structure is shown in Figure 4 and is similar to the feed design described in (Church *et al.* 1996). This design allows us to illuminate correctly the band defining filters and create an effective Faraday cage surrounding the bolometric detectors.

Each feed consists of a band defining filter stack mounted inside waveguide optics that couple the radiation from the tertiary mirror into an integrating bolometer cavity. The feed is divided in two parts separated by a 0.5 mm gap, one held at 2 K and the other at 300 mK.

The entrance horns are mounted in a horn positioning flange held at 2 K. Each horn couples to a section of waveguide with length  $2\lambda$  that acts as a high pass filter and rejects radiation with wavelength  $\lambda > 3.41a$ , where  $a$  is the radius of the waveguide. The 20' horns have an entrance aperture of 19.7 mm at  $f = 3.3$  and a waveguide diameter of 2.54 mm. The throughput is limited by a combination of the entrance aperture of the horns and the size of the Lyot stop to be  $A\Omega_{\text{total}} = 0.1 \text{ cm}^2\text{sr}$  for the 20' horns. This value is over the diffraction limit throughput  $A\Omega_{\text{horn}} \simeq \lambda^2 = 0.04 \text{ cm}^2\text{sr}$  at  $\lambda \simeq 2 \text{ mm}$  (150 GHz). The 40' horns have

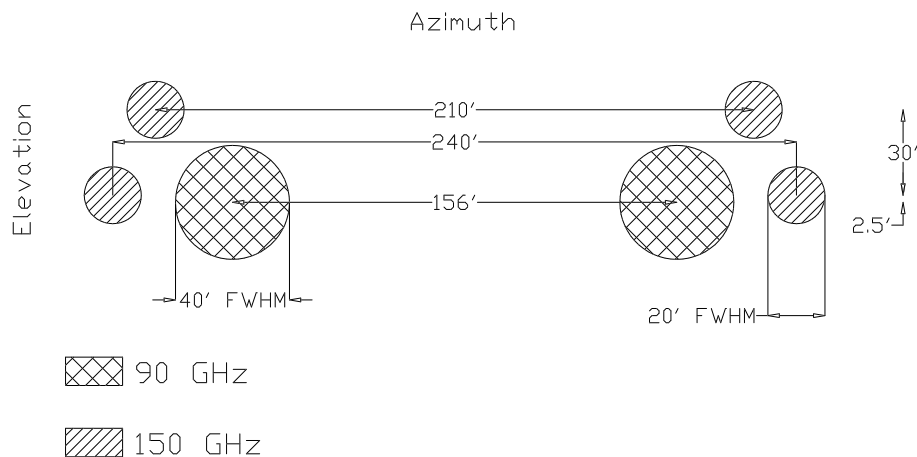


Fig. 3.— Location of the beams in the focal plane of the BNA photometer.

an entrance aperture of 33 mm and a waveguide diameter of 5.1 mm. These channels have approximately three times the throughput of the 20' channels with  $A\Omega \simeq 0.3 \text{ cm}^2\text{sr}$ , while the diffraction limit is  $0.1 \text{ cm}^2\text{sr}$ .

On the other side of the waveguide is an  $f/4$  conical horn that expands the waveguide to a diameter of 17.8 mm in the 20' channel and 27.9 mm in the 40' channel. At the end of this cone, the feed opens up to allow the mounting of a converging lens and an oversized metal mesh dichroic filter. A band pass filter followed by another identical converging lens and conical horn are held at 300 mK across the small gap of  $< 1 \text{ mm}$ . This final horn feeds a small cavity containing a micromesh bolometer which absorbs  $> 90\%$  of the radiation entering the cavity. In the geometrical limit, the lenses reimaging to infinity a point at the vertex of the horns on which they are mounted. In the diffraction limit, they each produce a beam waist at the center of the length of waveguide that contains the filters, thereby improving the coupling between the expanding horn at 2 K and the concentrating horn at 300 mK.

The spectral bands are defined by the 300 mK band pass filters, metal-mesh resonant grid filters with nominal central frequencies of 90 GHz and 150 GHz and 30% bandwidth.



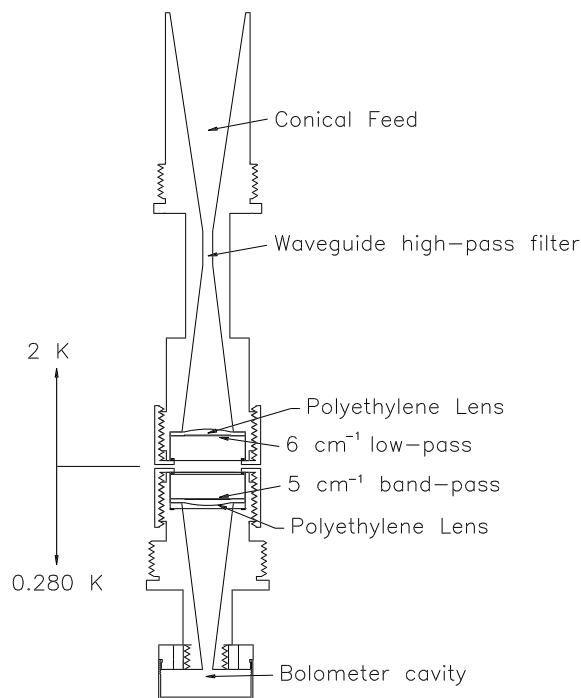


Fig. 4.— 150 GHz feed horn. The upper part is cooled at less than 2 K and the lower part to 0.280 K. See text for description.

These filters have high transmission in band with sharp band edges, but their performance degrades quickly as a function of off-axis angle. The  $f/4$  horns in the intermediate section of the feed structure insure that the filters are illuminated with small off-axis angles. The band pass filters also have a leak at approximately twice the central frequency. The 2 K dichroic filters in the feed structure eliminate these leaks and provide additional high frequency blocking with cutoff frequencies of 172 GHz for the 90 GHz channel and 217 GHz for the 150 GHz channel. The frequency response of a 90 GHz and a 150 GHz channel, measured with a Fourier Transform Spectrometer, are shown in Figure 5. The out-of-band transmission is  $< -25$  dB for  $\nu < 900$  GHz.

We have measured the optical efficiency of this structure equipped with filters for both 90 GHz and 150 GHz operation. The optical efficiency measurements were made using black

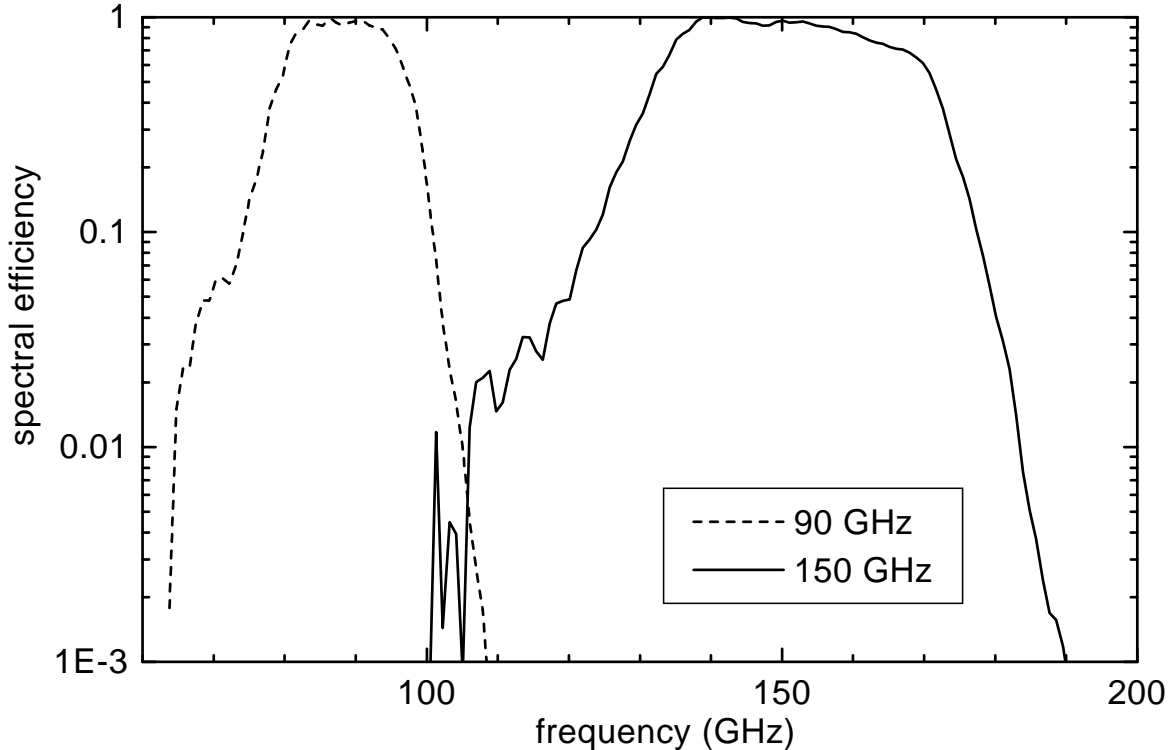


Fig. 5.— Frequency response of a 90 and a 150 GHz channel as measured with a Fourier Transform Spectrometer.

loads of eccosorb foam at 77 K and 300 K. We measure the difference in optical power on a bolometer by comparing the DC-coupled I-V curves of the detector under the different loading conditions. Pre-flight results are in Section 5.

Tables 2 and 3 give the band centroids and widths for the BOOMERANG photometers, along with the estimated loadings from the CMB, the telescope, and the atmosphere.

## 2.2. Detectors

BOOMERANG uses bolometers to detect the fluctuations in incoming radiation. A bolometer consists of a broadband absorber with heat capacity  $C$ , that has a weak thermal link  $G$ , to a thermal bath at a temperature  $T_b$ . Incident radiation produces a temperature rise in the absorber that is read out with a current biased thermistor. The sensitivity of a bolometer expressed in Noise Equivalent Power (NEP) is given by:

$$\text{NEP}_{\text{bolo}} = \gamma \sqrt{4kT_b^2 G} \quad (2)$$

$\nu_{nominal}$ (GHz)	$\nu_{peak}$ (GHz)	$\nu_0^{CMB}$ (GHz)	$\nu_0^{R-J}$ (GHz)	$\Delta\nu_{FWHM}$ (GHz)
90	88.5	93.6	94.1	33
150	136.5	155.7	157.9	54

Table 2: BOOMERANG North America Filter Bands.  $\nu_{peak}$  is the peak for a flat spectrum,  $\nu_0^{CMB}$  and  $\nu_0^{R-J}$  are respectively the peaks for a CMB and a Rayleigh-Jeans spectra.

	$\nu_{peak}$ (GHz)	$A\Omega$ $\text{cm}^2\text{sr}$	$P_{atm}$ (pW)	$P_{CMB}$ (pW)	$P_{tel}$ (pW)
BOOM/NA	88.5	0.3	0.004	0.10	0.42
	136.5	0.1	0.28	0.17	1.6

Table 3: BOOMERANG/NA in flight expected loadings

where  $\gamma$  is a constant of order unity that depends weakly on the sensitivity of the thermistor and  $k$  is Boltzmann’s constant. The dynamical equation for the temperature of the thermistor can be expressed as:

$$\frac{dT_{bolo}}{dt} = \frac{P_{in} - G(T_{bolo} - T_b)}{C} \quad (3)$$

where  $P_{in}$  is the incident power. From this equation, we can see that bolometers have a finite bandwidth limited by the time for the absorber to come to equilibrium after a change in incident power,  $\tau = C/G$ . Previous balloon-borne bolometric receivers have been limited in sensitivity or bandwidth by the properties of the materials used for fabrication of the detectors.

Bolometers are also limited in sensitivity by external sources of noise such as cosmic rays, microphonic disturbances, and Radio Frequencies Interference (RFI). Of particular importance for BOOMERANG is the cosmic ray rate on the Antarctic stratosphere, which is about an order of magnitude higher than at North American latitudes because the magnetic field of the earth funnels charged particles to the poles. We have experience of cosmic ray hits from many bolometric receivers flown at balloon altitude at temperate latitudes. The cosmic ray hit rate for the MAX experiment (Alsop *et al.* 1992) during a North American balloon flight was 0.14 Hz. In order to remove spurious signals from these cosmic ray interactions, cosmic rays were identified and a length of data corresponding to 10 detector time constants was removed. Because the MAX detector time constants were all less than 30 ms, this resulted in a loss of 5% of the data which did not severely affect the sensitivity. Almost half of the data would be contaminated by cosmic rays with the same detectors operated from a

Long Duration Balloon over the Antarctic.

In the North American flight of BOOMERANG we tested for the first time bolometers with a new architecture, consisting of a micromesh absorber with an indium bump-bonded NTD germanium thermistor. These bolometers can have lower heat capacity, lower thermal conductivities, lower cosmic ray cross section, and less sensitivity to microphonic heating than previous 300 mK bolometers. The micromesh absorbers and support structures are fabricated from a thin film of silicon nitride using microlithography. The absorber is a circular grid with 60-400  $\mu\text{m}$  grid spacing and 2-10% filling factor, metallized with 50 Å of chromium and 200 Å of gold. It is designed to efficiently couple to millimeter wave radiation and have low heat capacity and low cosmic ray cross section. Stiff mechanical support consists in strands of silicon nitride 1000  $\mu\text{m}$  long with 3-5  $\mu\text{m}^2$  cross sectional area connecting the absorber to a silicon frame, with a thermal conductivity of less than  $2 \times 10^{-11} \text{ W K}^{-1}$ . The design and construction of the micromesh absorbers as well as their optical and mechanical properties are described in (Mauskopf et al. 1997).

The thermistor is a rectangular prism of Neutron Transmutation Doped germanium 50  $\mu\text{m} \times 100 \mu\text{m} \times 300 \mu\text{m}$ , a factor of 10 times smaller volume than NTD thermistors typically used in composite bolometers. Using these small thermistors decreases the heat capacity of the bolometer by a factor of 5 and increases the fundamental microphonic frequency by a factor of 10. To allow the thermistor to be indium bump-bonded to the micromesh, one of the long faces of the NTD material is metallized with two pads 50  $\mu\text{m}$  wide at either end. Each pad is first implanted with boron and then sputtered with 200 Å of palladium and 4000 Å of gold. Electrical leads, gold pads, and indium bumps are patterned on the micromesh while the silicon nitride still has a solid backing of silicon. Gold pads and indium bumps are deposited at the center of the micromesh on a 300  $\mu\text{m} \times 300 \mu\text{m}$  solid square of silicon nitride. For electrical leads, 200 Å of gold is deposited on some of the support legs of the silicon nitride connecting the pads for the thermistor with large gold pads on the silicon frame. The thermistor is pressed onto the indium bumps and finally the silicon is etched from the back of the micromesh. The front of the silicon nitride is coated in wax to protect the chip and the metallization during etching. This technique minimizes the amount of material used for reading out the thermistors and therefore minimizes the heat capacity of the device. The indium bump-bonds have survived repeated thermal cycling. A draw of a micromesh bolometer is shown in Figure 6. The performance of bolometers with indium bump-bonded thermistors is described in (Bock *et al.* 1996).

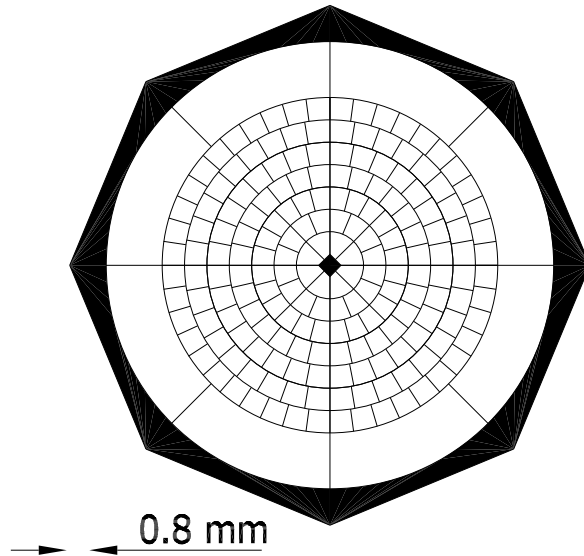


Fig. 6.— Schematic draw of a micromesh spider web bolometer absorber.

### 2.3. Readout Electronics

Most bolometric detectors in use today employ a high-impedance semiconductor thermistor biased with a constant current. JFET preamplifiers have been used to provide a combination of low voltage and current noise well matched to typical bolometer impedances (Halpern 1986), but exhibit excess voltage noise at frequencies typically below a few Hz and have limited the achievable bandwidth of these DC biased bolometers. At lower frequencies, drifts in the bias current, drifts in the temperature of the heat sink, and amplifier gain fluctuations have been expected to limit the ultimate stability of single bolometer systems.

AC bridge circuits have been successfully used in many experiments to read out pairs of bolometers with stability to 30 mHz (Wilbanks *et al.* 1990; Devlin *et al.* 1994). In this scheme a pair of detectors is biased with an alternating current so that resistance fluctuations are transformed into changes in the AC bias amplitude across each detector. These signals are differenced in a bridge, amplified and demodulated. The AC signal modulation eliminates the effects of  $1/f$  noise in the preamplifiers since the resulting signal spectrum is centered about the carrier frequency. The effects of drifts in the bias amplitude, amplifier gain, and heat sink temperature are greatly reduced if the two detectors in the bridge are well matched. The optical responsivity of each of the detectors in the bridge is equivalent to that of a detector biased with the same rms DC power and is constant in time as long as

the average power on the detector is constant over the course of one detector thermal time constant.

BOOMERANG employs an AC stabilized *total power* readout system for individual bolometers, mounted on a temperature regulated stage (Hristov *et al.* 2001a). The circuit is summarized in Figure 7.

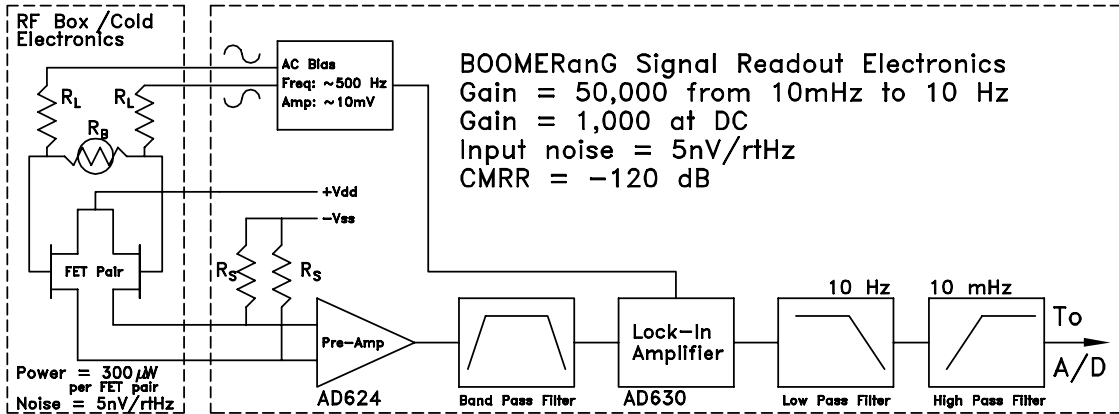


Fig. 7.— Block diagram of the bolometers readout electronics (one channel shown). The bolometer is AC biased with a differential, low-pass filtered square wave at  $\sim 500$  Hz. The AC voltage across the bolometer is modulated by the resistance variations induced by changes in the microwave power absorbed. A matched pair of low noise J-FETs inside the cryostat reduce the signal impedance from  $\sim 10\text{M}\Omega$  down to  $\sim 1\text{k}\Omega$ ; the signal is then amplified by a differential preamp (AD624), band-pass filtered to remove noise outside the signal bandwidth, and synchronously demodulated by a phase sensitive detector (AD630). The output of the AD630 is proportional to the instantaneous resistance of the bolometer. Signal components below 10 mHz are attenuated to get rid of  $1/f$  noise and drifts using a single pole high pass filter. High frequencies (above 10 Hz, i.e. above the cutoff frequency of the bolometer) are also removed by means of a 4-th order low-pass filter. The resulting signal is analog to digital converted with 16 bits resolution, at a sampling frequency of 62.5 Hz.

This system contains a cold J-FETs input stage (based on Infrared Laboratories TIA) and contributes less than  $10\text{ nVrms}/\sqrt{\text{Hz}}$  noise at all frequencies within the bolometer signal bandwidth down to 20 mHz. The warm readout circuit has a gain stability of  $< 10\text{ ppm}/^\circ\text{C}$ . We remove the large offset due to the background power on the detector with a final stage high pass filter with a cutoff frequency of 16 mHz. With this circuit, we have measured the noise spectrum of a low background micromesh bolometer with  $\text{NEP} = 1.2 \times 10^{-17}\text{ W}/\sqrt{\text{Hz}}$ , biased for maximum responsivity to be flat down to a frequency of 20 mHz.

## 2.4. RF Filtering

There are many sources of Radio Frequency Interference (RFI) on the balloon that could couple to bolometers. Microwave transmitters (400 MHz to 1.5 GHz, few W) that send the data stream to the ground and high current wires that drive the motors of the Attitude Control System (20 kHz PWM, several Amps) are situated within a few meters of the cryostat. The BOOMERANG wiring and focal plane are designed to prevent RFI from contributing to the noise of the bolometers.

The bolometers are contained inside a 2 K Faraday cage inside the cryostat. RFI can enter the cryostat through the optical entrance window and propagate into the 2 K optics box. However, the exit aperture of the optics box is RF sealed by the horn positioning plate. This plate contains feed horns with small waveguide apertures for radiation from the sky to pass through to the detectors. The largest waveguide feedthrough in this plate is 5.1 mm in diameter which corresponds to a waveguide cutoff of  $\sim 35$  GHz. Lower frequency RFI is reflected by this surface. Readout wires entering the bolometer Faraday cage can also propagate RF signals as coaxial cables. We run all of the bolometer wires through cast eccosorb filters mounted to the wall of the Faraday cage to attenuate these signals. The filters are 30 cm long and have a measured attenuation of  $< -20$  dB at frequencies from 20 MHz to a few GHz.

The readout electronics are also sensitive to RFI. We enclose all of the cryostat electronics in an RF tight box that forms an extension of the outer shell of the cryostat. The signals from the detectors pass through flexible KF-40 hose that is RF sealed to the hermetic connector flange on the cryostat and to the wall of the electronics box. The amplified signals exit the electronics box through *Spectrum* RF filters mounted on the wall of the box.

## 2.5. Cryogenics

A “heavy duty”  $^3\text{He}$  fridge and a large  $^4\text{He}$  cryostat have been developed specifically for the BOOMERANG experiment. A cutaway view of the cryostat is shown in Figure 8.

The main  $^4\text{He}$  cryostat has to be large enough to contain refocusing optics and a wide focal plane with several multiband photometers. The design and performance of the cryostat and refrigerator are described in detail elsewhere (Masi *et al.* 1998; Masi *et al.* 1999). The total volume occupied by the cryogenic section of the receiver is 69 liters. The design hold time is about 20 days; the helium tank volume is 60 liters, the nitrogen tank volume is 65 liters. Conduction thermal input is reduced by suspending both the tanks with Kevlar ropes (1.6 mm diameter). The vibration frequencies of these structures are all above 20 Hz,

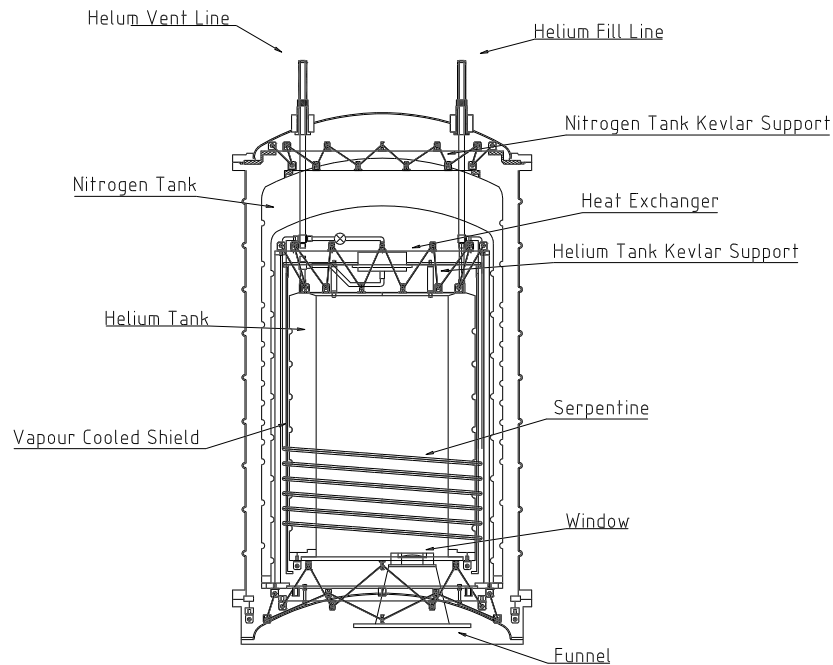


Fig. 8.— Main cryostat. The evaporating  $^4\text{He}$  gas flow through the serpentine and the heat exchanger to cool a copper shield that minimize the heat input on the main Helium bath. The tanks are supported by kevlar cord. Nitrogen lines are not shown.

and the amplitude of the vibrations excited during the flight is expected to be very small. Radiation thermal input on the nitrogen tank is reduced by means of 30 layers of aluminized mylar for superinsulation. The total thermal input on the nitrogen bath is  $6.6 \pm 0.4$  W.

The radiative thermal load on the  $\text{L}^4\text{He}$  is minimized by the use of a vapor cooled shield. As the liquid helium evaporates, the cold gas flows through a spiral tube that is soldered to the outside of a copper shield which surrounds the Helium tank and through a copper heat exchanger that is attached to the top of the vapor cooled shield before emerging from the cryostat. The temperature of the vapor cooled shield depends on the gas flow rate from the Helium tank. During normal operation, the shield remains at a temperature of 15-17 K. The total thermal input on the helium bath is linked to the radiative input through the cryostat window and in flight conditions is about 75 mW.

The cryostat has two circular windows 66 mm in diameter, made with  $50 \mu\text{m}$  polypropylene supported by an aluminum frame.



In the BNA flight we used Indium seals able to work at the very low temperature experienced during the night flight ( $-50^{\circ}\text{C}$ ). In the day-time LDB flight it was possible to use rubber (Buna-N) seals being the temperature of the dewar always  $> -30^{\circ}\text{C}$ .

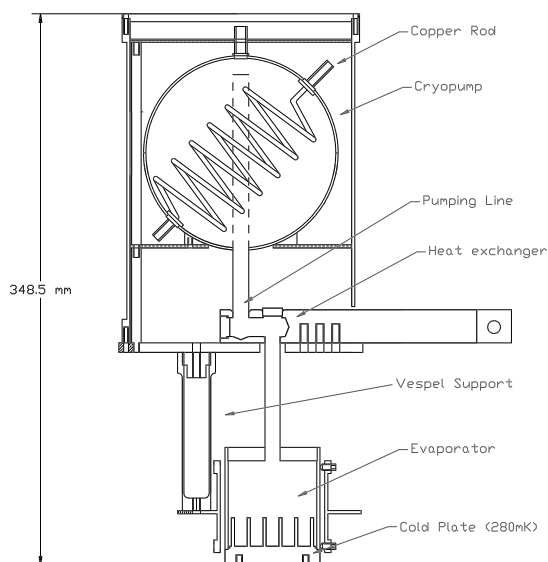


Fig. 9.— BOOMERANG  $^3\text{He}$  fridge. See description in the text. A mechanical thermal switch, not reported in the drawing, connects the cryopump to the heat exchanger flange.

The bolometers are cooled by a self contained  $^3\text{He}$  fridge shown in Figure 9. The fridge operates with a charcoal sorption pump and can be recycled electronically. During a cycle, hot  $^3\text{He}$  gas is expelled from the pump by heating it to  $\simeq 40\text{ K}$  with a resistance heater. This gas passes through a thin-walled stainless steel tube and condenses on a high purity copper condensation surface at  $\simeq 2\text{ K}$ . The  $^3\text{He}$  liquid then drops through another stainless steel tube into a  $125\text{ cm}^3$  evaporator pot. Finally, when all of the gas has collected in the evaporator, the heater power is removed from the pump and it is connected to the condensation point with a mechanical heat switch. The pump temperature drops to  $\sim 3\text{ K}$  and pumps on the liquid  $^3\text{He}$  in the evaporator, reducing its temperature to  $< 300\text{ mK}$ .

The pump is made of two stainless steel hemispheres crossed by a copper rod that extends outside, to provide thermal attachment points to both the heater and the thermal switch. The pump is connected to the copper condensation plate ( $\sim 2$  K) through a 1 cm diameter stainless steel tube. There is a 1 cm diameter hole that horizontally passes through the condensation plate, with a 1 cm path to provide more surface area to transfer heat from the  $^3\text{He}$  gas to the copper. The evaporator consists of a stainless steel cylinder with a 6 cm diameter copper endcap with a ring of 6 mm diameter bolt holes for thermal attachment. The charge is 34 liters STP at 40 bars. The heat load on the  $^3\text{He}$  stage is about  $20 \mu\text{W}$ . About half of this is due to thermal conduction from the condensation point to the evaporator through the 0.010" diameter stainless steel pump tube. The remaining  $10 \mu\text{W}$  is from the mechanical supports for the focal plane. The focal plane weighs 2.5 Kg and must be rigidly held with a mounting structure strong enough to withstand 10 G acceleration in any direction while providing minimal additional thermal input to the  $^3\text{He}$  fridge. We use four thin-walled vespel tubes to satisfy these requirements. Vespel has an extremely high strength to thermal conductivity ratio at temperatures from 0.3 to 2 K. The tubes are 1" in diameter, 0.030" thick and 3" long. The yield strength of a tube can be calculated from standard formulae. The criterion we use for strength is that the maximum deflection be less than 1% of the elastic limit of the material. Additional heat load from electrical leads is minimized by the use of 0.005" diameter manganin wires that run up the length of the vespel tubes between the cold JFET amplifier box and the detectors. The wires are firmly attached to fixed surfaces along their entire length with teflon tape to eliminate vibrations which can make the detectors microphonically sensitive. The length of the wires is minimized to reduce their contribution to the input capacitance at the JFETs. The RC cutoff frequency for a 5 M $\Omega$  detector impedance is measured to be  $> 2$  kHz, for an input capacitance of  $< 40$  pF.

During observations, the temperature of the focal plane can be maintained constant with a high precision temperature regulation circuit (Hristov *et al.* 2001b). In fact, temperature fluctuations of the 300 mK stage can contribute to excess bolometer noise. The temperature of the bolometer is determined by:

$$T_{\text{bolo}} = T_0 + \frac{P_{\text{opt}}}{\int_{T_0}^{T_{\text{bolo}}} \kappa_0 T^\alpha dT} \quad (4)$$

where  $P_{\text{opt}}$  is the optical power on the detector and  $\int_{T_0}^{T_{\text{bolo}}} \kappa_0 T^\alpha dT$ , indicated as  $G_{\text{eff}}$  ( $\text{W K}^{-1}$ ) hereafter, is the effective thermal conductivity per unit of temperature between the thermistor and the bath at  $T_0$ . Therefore the change in bolometer temperature for a change in base plate temperature is given by:

$$\Delta T_{\text{bolo}} = \beta \Delta T_0 \quad (5)$$

where  $\beta$  is a constant of order unity. The bolometer NEP is related to these temperature

fluctuations by:

$$\text{NEP}_T = G_{\text{eff}} \Delta T_{\text{bolo}} \tag{6}$$

where  $\text{NEP}_T$  is in  $\text{W}/\sqrt{\text{Hz}}$  and  $\Delta T_{\text{bolo}}$  ( $\text{K}/\sqrt{\text{Hz}}$ ) is the spectrum of temperature fluctuations. Therefore, the condition for temperature stability of the cold stage is  $\text{NEP}_T < \text{NEP}_{\text{bolo}}$ . For the BOOMERANG bolometers with  $G_{\text{eff}} = 8 \times 10^{-11} \text{ W K}^{-1}$  and  $\text{NEP}_{\text{bolo}} \simeq 2 \times 10^{-17} \text{ W}/\sqrt{\text{Hz}}$  the requirement for the stability of the cold stage is:

$$\Delta T_{\text{bolo}} < 250 \text{ nK}/\sqrt{\text{Hz}} \tag{7}$$

Two NTD thermistors are mounted on the 300 mK stage and read out with DC coupled bridge circuits. One channel is used as the control sensor and the other is a monitor sensor. We measure the spectrum of fluctuations from the monitor channel while the temperature regulation circuit is running to be flat down to  $< 30 \text{ mHz}$  with an amplitude of  $40 \mu\text{Vrms}/\sqrt{\text{Hz}}$  corresponding to a temperature stability of  $120 \text{ nK}/\sqrt{\text{Hz}}$ . This is better than is needed to insure that the BOOMERANG bolometers do not have a significant noise contribution from temperature fluctuations.

## 2.6. Pressure control systems

The pressure on the main helium bath is maintained around 10 mbar in lab and in flight to keep the bath temperature below 2 K, while the pressure on the nitrogen bath is kept around 1 atm to prevent the formation of fluffy solid. We used two pressurization systems. The helium pressurization system allows us to pump on the bath at ground and to open to atmosphere pressure at float by means of a motorized high vacuum seal valve. The nitrogen system controls the pressure using an absolute sensor and three electrovalves. Both systems have relief valves to allow safety and functionality even in the case of electronic failures.

## 2.7. Internal calibrator

An internal calibrator in the reimaging optics box allows us to monitor the detector sensitivity during flight. The calibrator consists of a high background bolometer with an NTD 4 Ge thermistor attached to the center of a 5.6 mm diameter Silicon Nitride absorber, electrically connected with 0.001” diameter copper leads. The calibrator is mounted on the 2 K stage directly behind a 1 cm hole in the center of the tertiary mirror, where all of the beams from the concentrating horns are coincident. The calibrator can be heated with a current pulse to give a temperature rise of several Kelvin with a recovery time of a few

milliseconds. The corresponding power on the detectors is:

$$P_{\text{cal}} \simeq 2k\Delta T_{\text{cal}} \frac{\nu^2}{c^2} \Delta\nu \cdot \Omega\epsilon f \quad (8)$$

where  $\epsilon$  is the calibrator efficiency and  $f$  is the effective Lyot stop fraction area filled by the calibrator. This corresponds to an equivalent signal on the sky of

$$\Delta T_{\text{CMB}} = \epsilon\Delta T_{\text{cal}}f \quad (9)$$

Response to the internal calibrator during flight for one of the detectors is shown in Figure 10. The equivalent signal on the sky is  $\sim 175$  mK.

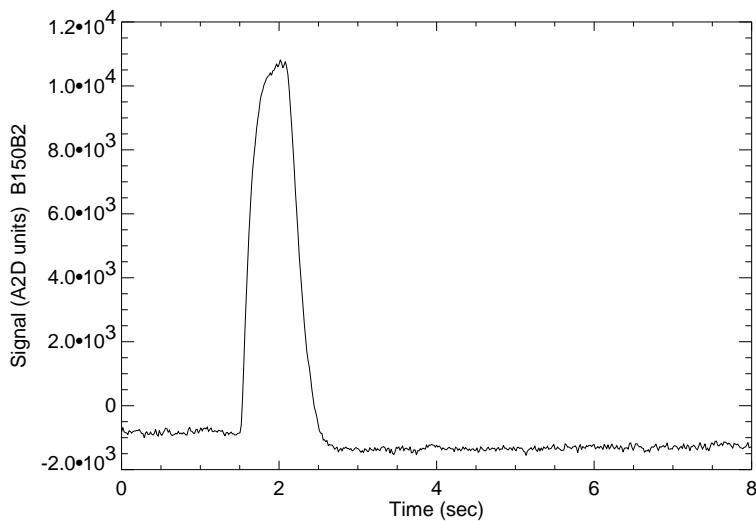


Fig. 10.— Bolometer signal during a pulse from the internal calibrator. A/D units are used, corresponding to a full scale of  $\pm 10$  Volts in 16 bits.

### 3. Attitude Control System

The Attitude Control System (ACS) must be able to point in a selected sky direction, and track it or scan over it with a reasonable speed. The specifications are 1 arcmin rms for pointing stability, with a reconstruction capability better than  $\sim 0.5$  arcmin maximum. Our main modulation is obtained scanning in azimuth, with a saw-tooth scan, with an amplitude of 40 deg (p-p) and a scan rate of about  $2 \text{ deg s}^{-1}$ . We have developed an ACS for BOOMERANG with these capabilities based on the ACS systems designed and built for the ARGO and MAX-5 experiments (deBernardis *et al.* 1993; Tanaka *et al.* 1995). The

BOOMERANG ACS is based on a pivot which decouples the payload from the flight chain and controls the azimuth, plus one linear actuator controlling the elevation of the inner frame of the payload. The pivot has two flywheels, moved by powerful torque motors with tachometers. On the inner frame, which is steerable in elevation with respect to the gondola frame, are mounted both the telescope and the cryogenic receiver. The observable elevation range is between 33 and 65 deg. The sensors are different for night (North America) and day (Antarctic) flights. For night flights we have a magnetometer and an elevation encoder; additional information on the average attitude is obtained by means of a sensitive tilt sensor. A CCD star camera is used outside the feedback loop for absolute attitude reconstruction. A CPU handles commands and observation sequencing; the same CPU digitizes sensor data, and controls the current of the three torque motors.

### 3.1. CCD Star Camera

We used a video CCD camera (*Cohu 4910*) with a large aperture lens (*Fujinon CF50L*) as a star sensor. The focal length is 50 mm, the numerical aperture is  $f/0.7$ . The CCD format is  $1/2''$  and the video signal is *RS-170* at 60 Hz. The image area in the CCD is  $6.4\text{mm} \times 4.8\text{mm}$ , with  $768 \times 494$  pixels. The resulting field angle is  $7.30^\circ \times 5.50^\circ$ . The optics are baffled to protect the lens input against stray rays from reflecting surfaces in the payload. The baffle is a corrugated cylindrical structure painted black on the internal surface and dimensioned for complete protection of the lens input. We removed the CCD protection glass in order to accommodate the lens output surface close enough to the CCD chip surface. Boresight between the star camera and the millimeter wave telescope is trimmed at ground, and cannot be changed in flight. The CCD is mounted on the gondola through fiberglass supports and is surrounded by a protective and thermally insulating foam box. A few resistors, dissipating a total of  $\sim 10$  W, are used to keep the system warm.

CCD images are processed on board in real time. We used a *Matrox Image-LC* board as a frame grabber and signal processing unit (DSP). The board accepts an analog (video) input and returns a VGA output image. The star sensor computer is connected to the other flight computers through serial ports. These electronics were assembled inside a pressure vessel in order to let the system operating at standard pressure during the flight. This is required for both the correct operation of the hard disk and the thermalization of the components. A thermostat and two fans inside the vessel control the internal air temperature. The total heat dissipation of the system is  $\sim 50$  W. When the fans are operating the heat dissipating devices are thermally connected to the outer shell of the vessel, radiating away the heat and effectively cooling the system. If the air gets too cold, the fans stop, effectively insulating

the system. In this way we can maintain the operation temperature close to 20°C during the flight, despite of the low temperature ( $\sim 230$  K) and pressure ( $\sim 3$  mbar). We used the *Matrox Imaging Library (MIL)* package for the in flight star recognition software in an optimized C code. The image analysis algorithm uses *blob analysis* to select the two brightest stars in the field. The system is able to compute and transmit the pixel and brightness information five times per second.

Before the flight we tested the performances of the CCD and of the optics in a vacuum chamber at room temperature and at  $T \simeq 240$  K. We found a small increase of the sensitivity of the CCD at lower temperature, while there is no detectable defocusing of the image.

The sensitivity of the camera was checked observing a star field from the Campo Imperatore Astronomical Observatory (at an altitude 2200 m above the sea level). It was possible to identify sources of magnitude  $m \leq 6.5$ , not far from the sensitivity we obtained during the flight.

When tested with suitable sources (i.e. stars with  $m \leq 4$  and negligible seeing, as at float), the camera produces very accurate positions of the target. Taking advantage of averaging insite in centroid determination, the accuracy of the coordinates of the selected target is close to 1/10 of a pixel ( $\sim 3$  arcsec).

The alignment of the CCD axis with the microwave beam was obtained by observing a strong chopped thermal source placed at a distance of  $\sim 120$  m and correcting for the parallax due to the offset between the mm-wave telescope and the camera (540 mm in the meridian axis, 640 mm in the horizontal axis). We also tested the tilt of the CCD field respect to the horizontal axis performing pure azimuthal scans on the same source. We reduced the tilt below 2-3 pixels along a  $6^\circ$  azimuthal scan.

Since not all frames have two stars present, the pointing was reconstructed between good frames by integrating the data from the gyroscopes (sampled at 10 Hz). This led to a precision of less than 1 arcmin rms in the pointing solution.

Pendulations of the gondola was monitored by roll and pitch gyroscopes. The typical power spectrum of the pitch fluctuations is reported in figure 11.

#### 4. Scan strategy

The BOOMERANG scan strategies are designed to obtain high signal to noise measurements of CMB anisotropies covering as wide a range of angular scales as possible, limited only by the functional bandwidth of the detectors. The maximum scan speed is limited by

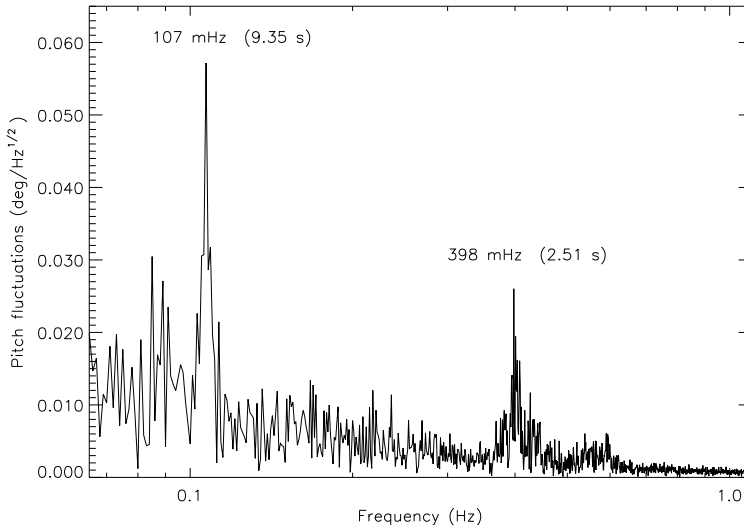


Fig. 11.— Power spectrum of the pitch of the payload during scans. Small pendulations are at 107 and 398 mHz corresponding to periods of 9.35 seconds (full flight chain) and 2.51 seconds (payload).

the mechanics of the Attitude Control System (ACS) and by the thermal time constant of the bolometers. The minimum scan speed is set by the stability of the detectors, readout electronics, and sources of local emission. The ratio of these maximum and minimum signal frequencies for the BOOMERANG detectors is  $\approx 30$  allowing us to cover a range in angular scale, corresponding to multipoles  $10 < \ell < 900$ .

The range of spatial frequencies, or multipole number  $\ell$ , that we sample depends primarily on the beam size. Because we use bolometric detectors, we are free to select any beam size at a given wavelength equal to or larger than the diffraction limit,  $\theta_{\text{diff}} = 1.22\lambda/D$  where  $D$  is the diameter of the illumination pattern on the primary that is fixed for all channels by the Lyot stop to be 85 cm. The throughput for such a system is a function of the beam size:

$$A\Omega(\lambda, \theta) = \lambda^2 \left( \frac{\theta}{\theta_{\text{diff}}} \right)^2 \quad (10)$$

The optical loading on the detector and the optimal thermal conductance,  $G$ , are proportional to the throughput,  $A\Omega$ . The absorbing area of the detectors also must be proportional to  $A\Omega$ , however the heat capacity,  $C$ , of the micromesh bolometers is dominated by the thermistor, so it is independent of throughput. Therefore, the time constant of optimized bolometers decreases as the beam size increases,  $\tau \propto 1/(A\Omega)$ . In addition, the signal from the CMB is proportional to the throughput but the detector noise increases like the square root, so that the sensitivity to CMB fluctuations improves like  $\sqrt{A\Omega}$ . Therefore, overmoded bolometers

are faster and more sensitive than diffraction limited channels. We can make use of this to scan faster and cover a larger area of sky with overmoded channels with high sensitivity and scan slower and obtain higher angular resolution with diffraction limited channels. We have optimized each BOOMERANG focal plane for angular resolution and sensitivity.

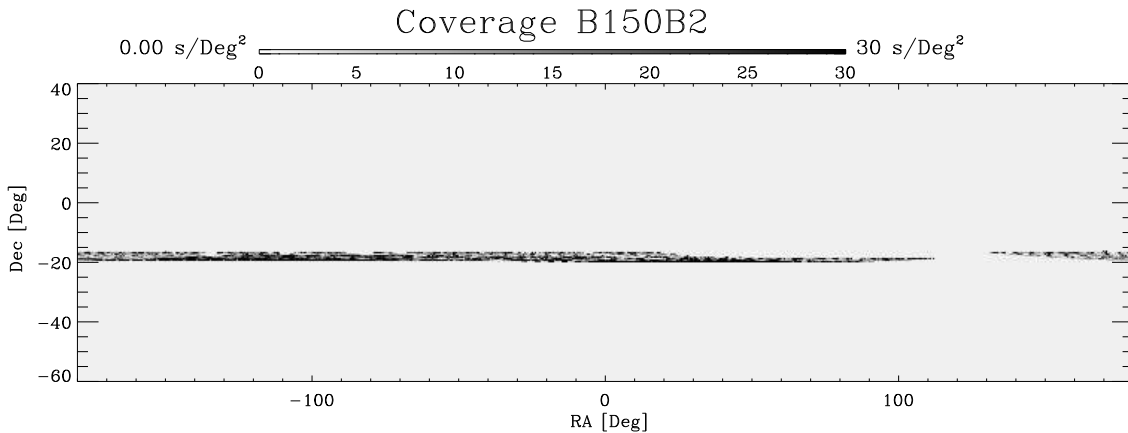


Fig. 12.— Sky coverage and integration time distribution during the flight of 1997, August 30.

The BOOMERANG North American flight, in 1997 August, covered a region of sky approximately 700 square degrees (figure 12). This region was selected to have a low column density of dust as estimated from the IRAS 100  $\mu\text{m}$  measurements and provided even sky coverage with an appropriate integration time per pixel based on our detector sensitivity estimates. The focal plane shown in Figure 3 contained two 40' pixels at 90 GHz and four 20' pixels at 150 GHz. The gondola was scanned continuously in a triangle wave with peak to peak amplitude of 40 degrees and a maximum scan velocity of  $2 \text{ deg s}^{-1}$  corresponding to  $\sim 2$  bolometer time constants per beam.

## 5. Pre-Flight Calibration

The pre-flight calibration procedure is performed before declaring flight-readiness, in order to have a precise forecast of the flight performance of the instrument. For our telescope and receiver the most important tests are:

1. Bolometers load curves under different radiative loads. This is performed filling the photometer beam with blackbody loads at room temperature and at 77 K, and inserting



in the beam a cold attenuator, with 1% transmission, to simulate the in-flight radiative background. Results for throughput and optical efficiency are in Table 4.

Channel	throughput (cm <sup>2</sup> sr)	optical efficiency
NA-B150A1	0.11	8%
NA-B150A2	0.08	19%
NA-B150B1	0.11	8%
NA-B150B2	0.08	20%
NA-B90A	0.27	7%
NA-B90B	0.27	9%

Table 4: Pre-flight throughput and optical efficiency calibration for the six detectors

2. Voltage noise measurements of the system were performed to estimate the sensitivity and to check for 1/f noise in the detectors. Results in Table 5. Also a preliminary measure of the detectors time constants  $\tau$  was done to have an indication of performance. This measurement has to be repeated in flight in order to have the correct values, strongly dependent on the background radiation (see section 6.1)

Channel	Noise $nV/\sqrt{Hz}$	1/f knee Hz	Responsivity V/W	NEP $W/\sqrt{Hz}$	NET <sub>CMB</sub> $\mu K\sqrt{s}$
NA-B150A1	12	0.8	$4.5 \cdot 10^8$	$2.6 \cdot 10^{-17}$	260
NA-B150A2	12	0.2	$3.1 \cdot 10^8$	$3.8 \cdot 10^{-17}$	220
NA-B150B1	16	0.5	$4.4 \cdot 10^8$	$3.6 \cdot 10^{-17}$	360
NA-B150B2	11	< 0.1	$3.6 \cdot 10^8$	$3.1 \cdot 10^{-17}$	160
NA-B90A	12	0.8	$4.7 \cdot 10^8$	$2.6 \cdot 10^{-17}$	210
NA-B90B	14	0.8	$3.5 \cdot 10^8$	$4.0 \cdot 10^{-17}$	240

Table 5: Pre-flight voltage noise measurements

3. Spectral characterization was made using a Lamellar Grating Interferometer with a Hg Vapor Lamp as Rayleigh-Jeans source. A check for near-band leak in the optical filters was made by means of three thick grill filters at 4.9, 7.7 and 10.5 cm<sup>-1</sup>, which reduced the integrated signal by more than a factor 100 in the corresponding bands.
4. Beam profiles were measured using a collimated source, filling the telescope acceptance area. The wide (1 meter diameter) parallel beam is produced by a thermal source in the focus of a large parabolic reflector.

5. Sidelobes measurements or upper limits. We have illuminated the fully integrated payload using a high power (30 mW) 90 GHz Gunn oscillator, completed with calibrated attenuators and high gain horn (20 deg FWHM). The microwave source was electronically chopped at 11 Hz. The payload was located at the center of a wide, flat area, and the source was setup at a distance of  $\sim 50$  m from the payload, at an apparent elevation of  $\sim 39$  degrees, so that the microwave beam over-illuminated the payload. We first boresighted the BOOMERANG telescope to the fully attenuated microwave source, to record the axial gain of the instrument. We then rotated the payload in azimuth, reducing the source attenuation as necessary, to record the far sidelobe response of the instrument for different off-axis locations of the source. We made several spins, with different apparent elevations of the source. Results for a sample elevation are reported in Figure 13.

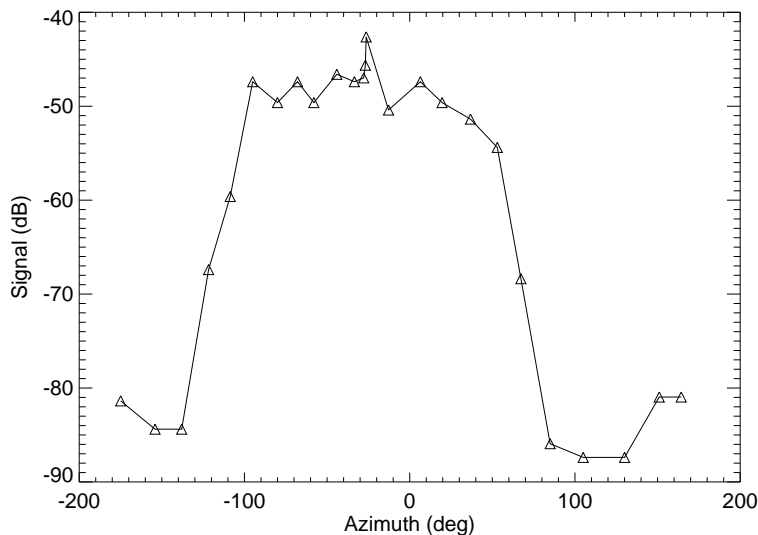


Fig. 13.— Sidelobes measurements at ground. The source is positioned at an elevation of 39 deg, while the telescope is pointed at 49 deg during this scan. The sharp cutoff at large angles is due to the effect of the large sun shields.

## 6. Observations and in flight performances

The system was flown for 6 hours on 1997 August 30 from the National Scientific Balloon Facility in Palestine, Texas. All the subsystems performed well during the flight: the He vent valve was opened at float and was closed at termination, the Nitrogen bath was

pressurized to 1000 mbar, the  $^3\text{He}$  fridge temperature (290mK) drifted with the  $^4\text{He}$  temperature by less than 10 mK during the 7.5 hours of the flight, with a maximum temperature of 300 mK before venting to atmosphere and slowly drifting down to 290 mK. The main  $^4\text{He}$  cryostat warmed to 2.05 K during ascent and then recovered to 1.65 K. Pendulations were not generated during CMB scans at a level greater than 0.5 arcmin, and both azimuth scans at  $2 \text{ deg s}^{-1}$  (see Figure 14) and full azimuth rotations (at 2 and 3 rpm) of the payload were performed effectively. The loading on the bolometers was as expected, and the bolometers were effectively CR immune, with white noise ranging between 500 and 1000  $\mu\text{K}/\sqrt{\text{Hz}}$ .

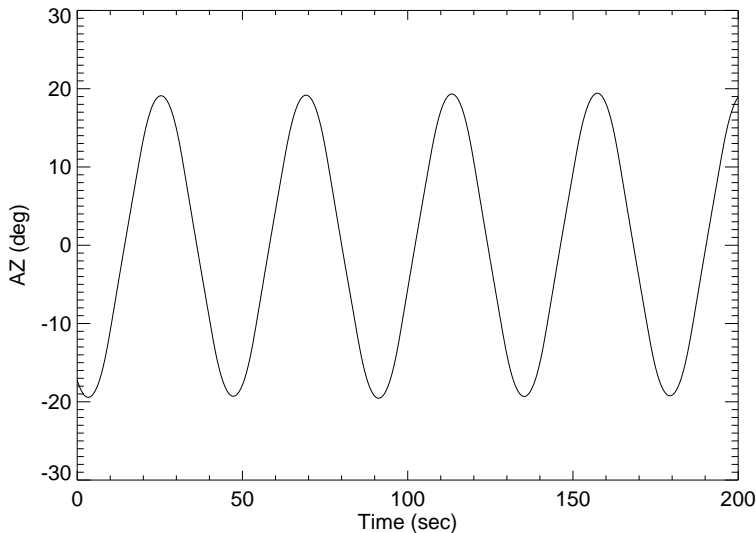


Fig. 14.— Azimuth read by the magnetometer during a scan. The amplitude is  $\pm 20$  deg, the shape is a smoothed saw tooth function. In this configuration the fraction of the scan at constant speed fraction is about one half of the total.

Measurements of the in flight performance (time constants, beam mapping and calibration constants) are essential to a good determination of the power spectrum of the anisotropies. The measured power spectrum is in fact the convolution of the real power spectrum with an angular function given by the shape of the beam (see Figure 15) and the amplitude of the spectrum depends on the calibration constant.

### 6.1. In-flight time constants of the bolometers

The total transfer function of the system is the combination of the electronics and the bolometer transfer functions. A high pass filter ( $\tau \sim 10 \text{ s}$ ) and a two pole Butterworth low pass filter determine the electronic transfer function, which was measured in lab. From

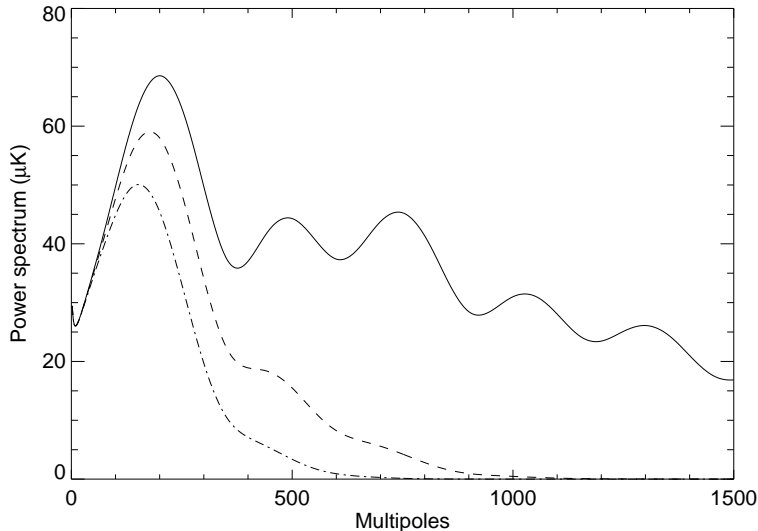


Fig. 15.— Convolution of the best fit power spectrum of CMB anisotropy (Mauskopf *et al.* 2000) with the BNA beams. The continuum line is the original power spectrum, the dashed line is the convolution with a 150 GHz channel(16.6 arcmin FWHM) and the dash-dotted line is the convolution with a 90 GHz channel (26.0 arcmin FWHM). The importance of a good determination of the beam shape is evident.

equation (3) we see that the bolometer behaves like a low pass filter with a time constant  $\tau = C/G$ . The value of  $\tau$  changes with the temperature of the receiver and with the radiative input, and has to be measured in flight. For a given input ( $IN(t)$ ) on the bolometer, the output ( $OUT(t)$ ) of the system with transfer function  $T(\omega)$  (bolometer and electronics) is

$$OUT(t) = IFT(FT(IN(t)) \cdot T(\omega)) \quad (11)$$

where  $FT$  and  $IFT$  are the Fourier Transform and Inverse Fourier Transform operator respectively. It is possible to fit the parameters in the  $T(\omega)$  using the  $OUT(t)$  data. As input we use the signal from a planet in a fast scan mode. When the scan speed is 3 rpm ( $18 \text{ deg s}^{-1}$ ) the time of transit of the planet in the beam ( $< 40'$ ) is about the time of two samples (sampling rate is 62.5 Hz). So the  $IN(t)$  signal has to be modeled with a beam shape function. Simulations show that for this sample rate and scan speed the results are the same within the error, assuming either gaussian or square beam. The measured time constants are reported in Table 6. These values are longer than expected for spider web bolometers. The source of the problem was tracked to excess heat capacity of the chromium layer, and was corrected for the devices used in the subsequent LDB flight.

channel	Time constant (ms)
NA-B150A1	$102 \pm 11$
NA-B150B1	$83 \pm 13$
NA-B150B2	$83 \pm 12$
NA-B90A	$165 \pm 9$
NA-B90B	$71 \pm 8$

Table 6: In-flight time constants of the BOOMERANG NA bolometers. All values except NA-B150B2 are calculated from fast scans across Jupiter. The NA-B150B2 value is calculated by comparing that detector’s cosmic ray signals with those of NA-150B1, which are the same to within error.

### 6.2. Jupiter calibration and beam mapping

During the August, 1997 North American flight of BOOMERANG, we calibrated the instrument and produced a detailed beam map by scanning the planet Jupiter (deBernardis *et al.* 1999). In addition, we made a secondary calibration through measurements of the CMB dipole, which is known to  $\simeq 1\%$  accuracy from the measurements of the COBE satellite (Kogut *et al.* 1993).

The responsivity of the instrument is defined as

$$\mathcal{R} = \frac{\Delta V}{\Delta W} \tag{12}$$

Where  $\Delta W$  is the radiative input and  $\Delta V$  the output of the bolometers. The calibration constant directly converts the signal in Volt into CMB temperature (in Kelvin) and is defined as

$$\mathcal{K} = \frac{\Delta V}{\Delta T_{CMB}} \tag{13}$$

The use of planets for calibration is a standard in mid latitude CMB experiments. Planets are bright sources, and their mm-wave brightness temperature is known at the 5% level. Moreover, they are point-like sources when compared to our beam, so they are perfectly suitable for mapping the shape of the beam pattern of the telescope.

The signal from the planet is

$$\Delta V_{planet} = \mathcal{R} A \Omega_{planet} \int E(\nu) B B(T_{eff}, \nu) d\nu \tag{14}$$

where  $T_{eff}$  is the brightness temperature of the planet,  $E(\nu)$  is the spectral efficiency and  $\Omega_{planet}$  is the (small) solid angle filled by the planet as computed from the ephemerides on the

day of the observation. The CMB signal is related to the derivative of the Planck function with respect to the temperature:

$$\Delta V_{CMB} = \mathcal{R}A\Omega \frac{\Delta T_{CMB}}{T_{CMB}} \int E(\nu)BB(T_{CMB}, \nu) \frac{xe^x}{e^x - 1} d\nu \quad (15)$$

where  $A\Omega$  is the throughput of the system,  $x = h\nu/kT_{CMB}$  and  $BB(\nu, T)$  is the Planck function. Note that the beam solid angle  $\Omega$  is the angular response function  $RA(\theta, \Phi)$  integrated over all the angles :

$$\Omega = \int_{4\pi} RA(\theta, \Phi) \cos \theta \sin \theta d\theta d\Phi \quad (16)$$

From the (14) and the (15) the resulting expression for the calibration constant is:

$$\mathcal{K} = \frac{\Delta V_{CMB}}{\Delta T_{CMB}} = \frac{\Delta V_{planet}}{T_{CMB}} \frac{\Omega}{\Omega_{planet}} \frac{\int E(\nu)BB(T_{CMB}, \nu)xe^x(e^x - 1)^{-1}d\nu}{\int E(\nu)BB(T_{eff}, \nu)d\nu} \quad (17)$$

$E(\nu)$  has been measured in laboratory,  $\Delta V_{planet}$  is the maximum signal from the planet and  $\Omega$  can be determined from a raster scan on the planet.

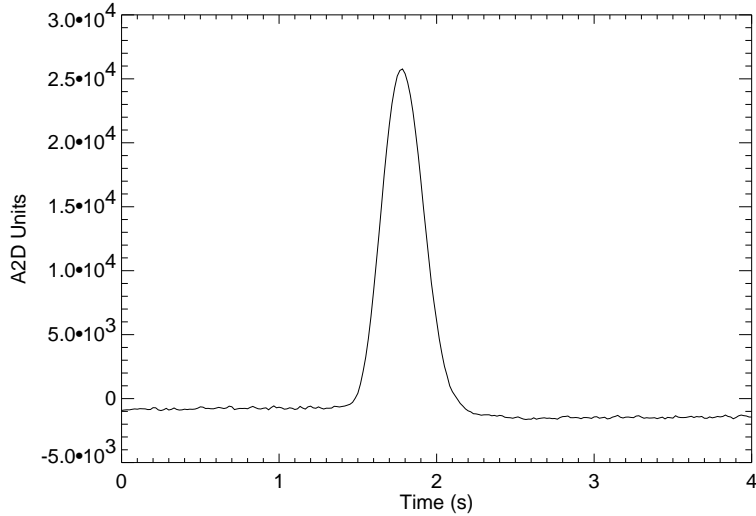


Fig. 16.— Raw data of a single scan on Jupiter at 150 GHz. S/N is  $> 100$ , scan speed is  $1.1 \text{ deg s}^{-1}$ . The negative tail of the data is due to the AC-coupling of the signal.

The telescope made two series of scans on Jupiter with an amplitude of  $15 \text{ deg}$  and a speed of  $1.1 \text{ deg s}^{-1}$ . Jupiter has an effective source temperature of  $T_{eff} = (173 \pm 9) \text{ K}$  (Ulich 1981; Goldin et al. 1997). The data have a high signal to noise ratio ( $> 100$ ) (see Figure 16) and permit to produce the beam profile of each receiver. The solid angles  $\Omega$  are

computed integrating the angular response,  $RA(\theta, \Phi)$ , given by the pixellized Jupiter map. Errors are given by the pointing error and the noise. The beams are symmetric with minor and major axes equivalent within 5%. FWHM are computed averaging the data in annuli around the center and fitting the shape with a gaussian function (see Figure 17).

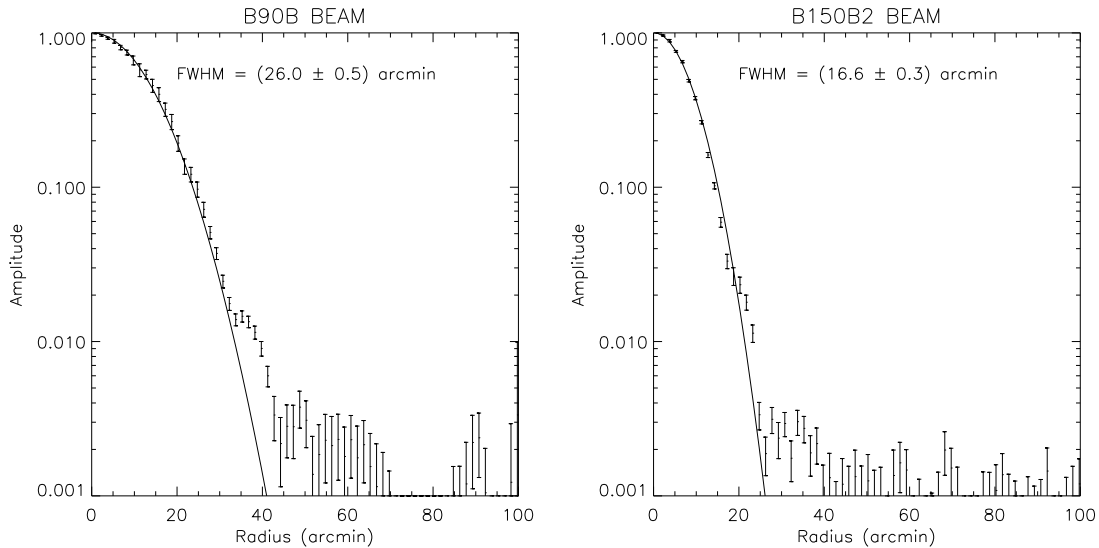


Fig. 17.— Jupiter data averaged in annuli around the centroid and gaussian fits. The small shoulders evident at a few percent level are real and are due to aberrations in the optical system.

Solid angles and FWHM are summarized in Table 7. The calibration constants are in Table 8.

channel	FWHM (arcmin)	$\Omega(sr)$
NA-B150A1	19.5	$(3.04 \pm 0.17)10^{-5}$
NA-B150B1	19	$(3.03 \pm 0.25)10^{-5}$
NA-B150B2	16.6	$(2.63 \pm 0.10)10^{-5}$
NA-B90A	24	$(5.61 \pm 0.36)10^{-5}$
NA-B90B	26	$(6.47 \pm 0.27)10^{-5}$

Table 7: Beam size measurements for the BOOMERANG NA telescope.

channel	$\mathcal{K}_{Jupiter}(nV/mK)$	$\mathcal{K}_{dipole}(nV/mK)$
NA-B150A1	$57.1 \pm 5.1$	$54.1 \pm 3.2$
NA-B150B1	$59.9 \pm 7.8$	$53.0 \pm 2.1$
NA-B150B2	$71.4 \pm 5.7$	$66.4 \pm 1.5$
NA-B90A	$48.1 \pm 8.2$	$43.1 \pm 1.1$
NA-B90B	$60.9 \pm 8.5$	$61.9 \pm 2.5$

Table 8: Calibration constants for the BOOMERANG NA telescope. The dipole calibration comes from the set of revolutions immediately after the Jupiter calibration.

### 6.3. Dipole calibration

The dipole (Fixsen *et al.* 1994) is a well calibrated source, featuring the same spectrum as CMB anisotropies and completely filling the beam of CMB anisotropy experiments. It is available at any time during the observations, thus allowing repeated checks for the calibration of the experiment. If a scanning experiment can perform large scale scans, the dipole will appear as a scan synchronous signal with an amplitude  $\Delta T_{dipole}$  of the order of a few mK (depending on the actual scan geometry), thus perfectly suitable for calibration. The calibration constant is simply

$$\mathcal{K} = \frac{\Delta V_{dipole}}{\Delta T_{dipole}} \quad (18)$$

where  $\Delta V_{dipole}$  is the amplitude of the signal during dipole observations. The precision of this measurement is affected by the presence of atmospheric emission and by 1/f noise of the system. The BNA bolometers showed noise spectra white down to 10 mHz. In these conditions it is possible to make dipole scans with a period of the order of a minute without being significantly affected by 1/f noise.

Dipole scans consisted in full azimuth revolutions of the gondola at  $18 \text{ deg s}^{-1}$  and were carried out for 10 minutes every hour. The instantaneous signal to noise ratio of the dipole scans was  $\sim 3$ . Raw data from one of the dipole scans are shown in Figure 18.

In Figure 19 we plot the azimuth of the maximum dipole signal versus the azimuth of the CMB dipole as observed from the payload position at the time of the observations, thus providing evidence for detection of the CMB dipole, and convincingly rejecting any hypothesized local origin of the signal.

The CMB dipole calibration in the first set of revolutions is consistent with Jupiter calibration performed immediately before (see Table 8). We note however that the dipole signal shape and size changes in the subsequent set of rotations for both B90B and B150B2 chan-



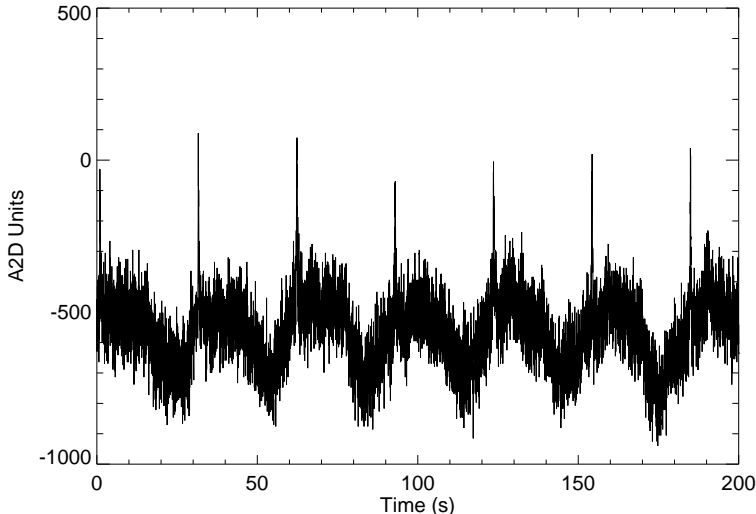


Fig. 18.— Raw data of a fast rotation. The CMB dipole produces a sinusoidal signal. The spike at regular phase is the signal from Jupiter used for time constant measurements. Full rotations of the payload have been repeated 4 times during the flight, at intervals of more than one hour.

nels, producing calibrations not completely consistent with those derived from the internal calibrator (see Figure 20).

Even if the atmospheric emission is greatly reduced at balloon altitude ( $> 35$  km), large scale fluctuations of the atmospheric brightness could be non-negligible with respect to the CMB dipole, thus giving a contamination at large scales hard to remove without a monitoring high frequency (240, 400 GHz) channel (Page *et al.* 1990; Lee *et al.* 1999). For this reason we have used the Jupiter calibration and the internal calibrator transfer for the data analysis of this flight of BOOMERANG.

#### 6.4. In flight noise

In flight noise performance is measured computing the power spectrum of the bolometers signals after de-spiking and deconvolution, avoiding data taken when the gondola inverts the scanning direction (turnarounds). Noise equivalent temperatures (NET) are calculated using in flight calibration constants. In flight noise includes bolometer noise, electronics noise, signal from the atmosphere, radio frequency noise, signal from the Galaxy and signal from the CMB. Results are in Table 9. Power spectra are reported in Figure 21 for the channels used in the analysis.

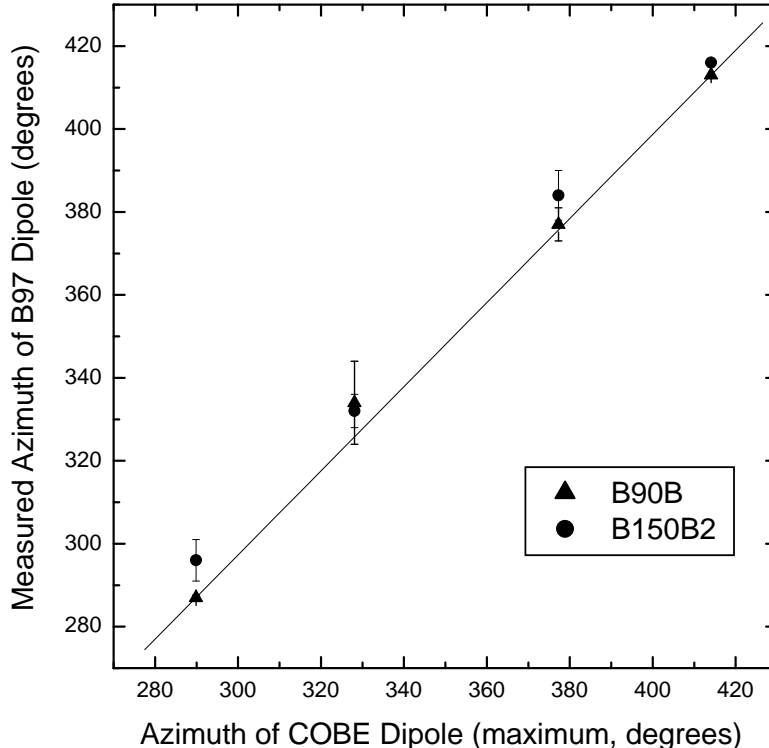


Fig. 19.— Azimuth of the maximum signal versus azimuth of the expected dipole direction during fast rotations. The good correlation is a proof that the signal is originated by the CMB dipole and it is not a local effect.

## 7. Sensitivity and Data Analysis

The sensitivity of a receiver to fluctuations in sky brightness at different angular scales can be represented by a window function. The shape of the window function depends on the details of the measurement. Calculations have been made for the window functions of different experiments (e.g. (White *et al.* 1994)) taking into account different beam shapes and sizes, chopping strategies, signal processing electronics, and data analysis strategies. Because of the complex chopping strategies employed to obtain stable offsets in these experiments, the window functions are often complicated. Recent experiments attempt to use specially tailored filters to generate multiple well-defined window functions from a single chop (Big Plate, MSAM). In addition, upcoming space missions will attempt to make fully reconstructed maps of diffuse millimeter-wave emission (MAP, Planck). For all of these experiments, the scan strategy is driven by the achievable bandwidth of the detectors which limits the maximum and minimum scan speed.

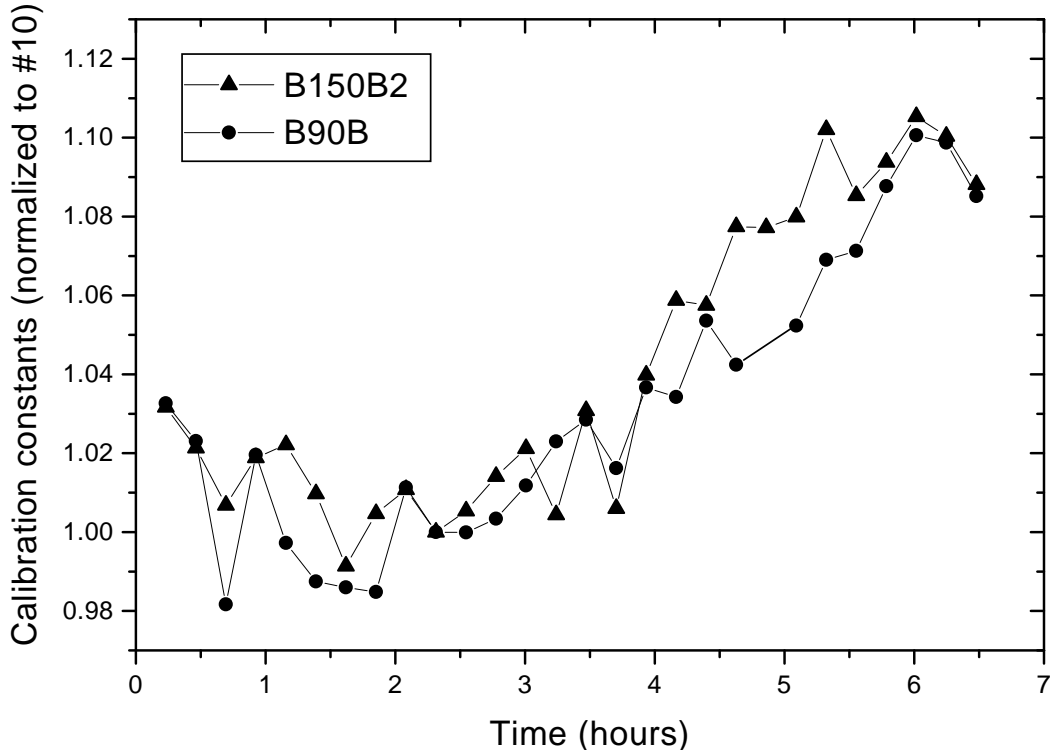


Fig. 20.— Fractional responsivity variations during the flight as measured from the internal calibrator signals, for both the channels used in the analysis. Starting from the second hour of flight the variations are less than 10%. The first two hours aren't used in the data analysis.

In BOOMERANG we have designed our scan strategy and beam size to utilize the full bandwidth and sensitivity of our detectors. The scan speed for both flights of BOOMERANG is matched to the signal bandwidth of the detectors and the sensitivity to large angular scales is limited by the stability of the readout electronics and atmospheric fluctuations. BOOMERANG can operate in either total power mode with the data from each detector analyzed independently, or in chopped mode, differencing between symmetric pixels in the focal plane to remove common mode noise sources. In total power mode, the window function of each channel is limited only by the beam size and the scan length. In differenced mode, the window function is determined by the beam size and beam separation in the focal plane.

The data from the BNA flight have been analyzed as a pixellized map with an experimentally determined correlation matrix describing the noise.

Maps of the B150B2 and B90B channels are in Figure 22. The  $\sim 25000$  pixels maps are noise dominated. These maps are produced just filtering the Time Ordered Data and

coadding the data in pixel with the HEALPix scheme<sup>11</sup>. The map produced to compute the anisotropies power spectrum was made using the MADCAP software package<sup>12</sup>. The noise correlation function is estimated from the time ordered data assumed to be noise dominated.

This analysis, described in (Mauskopf *et al.* 2000), lead to an error on the power spectrum measurements of  $\sim \pm 15 \mu\text{K}$  at 68% confidence level for band powers averaged over  $\Delta\ell = 50$  bins, centered at 6 multipoles covering the range  $25 < \ell < 325$ .

## 8. Conclusions

The feasibility of extended (many hundred square degree), resolved (20' FWHM), sensitive CMB maps using quasi-total-power balloon-borne microwave photometers has been demonstrated with the BOOMERANG/NA instrument. Critical technologies have been developed in several areas: spider web bolometers, total power readout electronics, low sidelobe response telescope, long duration cryogenics, and a scan-oriented attitude control system.

The BOOMERANG/LDB (Crill *et al.* 2001) payload makes optimal use of the technologies described here providing the first high signal to noise ratio map (de Bernardis *et al.* 2000) of a wide portion of the microwave sky.

## 9. Acknowledgements

The BOOMERANG experiment has been supported by Programma Nazionale di Ricerche in Antartide, Università di Roma “La Sapienza”, and Agenzia Spaziale Italiana in Italy,

---

<sup>11</sup><http://www.eso.org/kgorski/healpix/>

<sup>12</sup><http://cfpa.berkeley.edu/~borrill/cmb/madcap.html>

Channel	NET <sub>CMB</sub> ( $\mu\text{K}/\sqrt{\text{Hz}}$ )
NA-B150A1	700
NA-B150B1	1000
NA-B150B2	500
NA-B90A	1000
NA-B90B	740

Table 9: Noise Equivalent Temperature measured in flight.

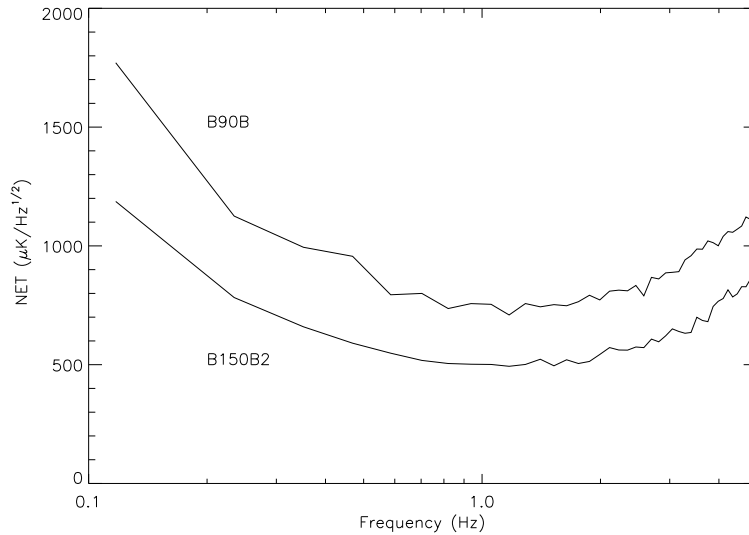


Fig. 21.— Noise Equivalent Temperature versus frequency for the two channels used in the analysis of the angular power spectrum of the CMB. At low frequencies  $1/f$  noise dominates. The rise at high frequencies is due to the bolometer time constants: the receiver loses sensitivity and the NET is increased after deconvolution. The most interesting frequencies are around 1.5 Hz where is expected to be the first peak of the anisotropies in the CMB (with scan speed of  $2 \text{ deg s}^{-1}$  at the elevation of 41 deg).

by NSF and NASA in the USA, and by PPARC in the UK. Doe/NERSC provided the supercomputing facilities. We acknowledge the use of HEALPix.

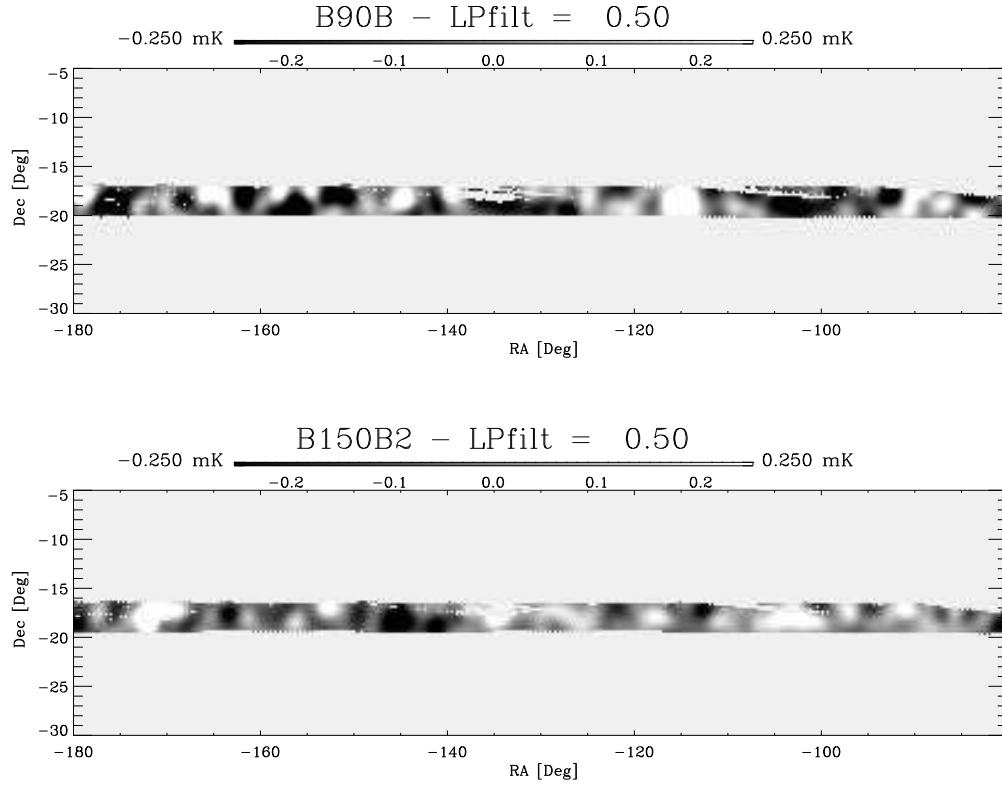


Fig. 22.— Maps of the measured flight from B150B2 and the B90B channels. Both maps are smoothed with a 0.5 deg FWHM gaussian in order to increase the signal to noise ratio. The structures in the maps are only partially concordant, showing that these maps are noise dominated rather than signal dominated. For better visualization only a portion of the full map (see coverage in Figure 12) is reported here.

## REFERENCES

- Alsop, D. C., Inman, C., Lange, A. E., and Wilbanks, T. 1992, *Applied Optics*, 31, 6610
- Bock, J. J. *et al.* 1996, Proc. 30th ESLAB Symp. Submillimetre and Far-Infrared Space Instrumentation, ESTEC, Noordwijk, Netherlands, ESA SP-388.
- Bond, J. R., Crittenden, R., Davis, R. L., Efstathiou, G., Steinhardt, P. J. 1994, *Phys. Rev. Lett.*, 72, 13, astro-ph/9309041
- Church, S. E., Ganga, K. M., Holzappel, W. L., Ade, P. A. R., Mauskopf, P. D., Wilbanks, T. M., and Lange A. E. submitted to *Ap. J.*
- Crill, B. P. *et al.* 2000, in preparation.
- de Bernardis, P., Aquilini, E., Boscaleri, A., De Petris, M., Gervasi, M., Martinis, L., Masi, S., Natale, V., Palumbo, P., Scaramuzzi, F., Valenziano, L., 1993, *Astron. Astrophys.* 271, 683
- deBernardis, P., DeTroia, G., Miglio, L., 1999, *New Astronomy Review*, 43, pag. 281-287
- deBernardis, P. *et al.* , 2000, *Nature* , 404, pag. 955-959, astro-ph/0004404
- Devlin, M. J., Clapp, A. C., Gundersen, J. O., Hagmann, C. A., Hristov, V. V., Lange, A. E., Lim, M. A., Lubin, P. M., Mauskopf, P. D., Richards, P. L., Smoot, G. F., Tanaka, S. T. 1994, *Ap. J.* , 433, L57, astro-ph/9404036
- Fixsen, D. J., *et al.* 1994, *Ap. J.* , 420, 445
- Goldin, A. B., *et al.* 1997, *Ap. J. Lett.* , 488, 161
- Gundersen, J. O., Clapp, A. C., Devlin, M. J., Holmes, W., Fischer, M. L., Meinhold, P. R., Lange, A. E., Lubin, P. M., Richards, P. L., *et al.* 1993, *Ap. J.* , 413, L1
- Halpern, M., Gush, H.P., Wishnow, E., De Cosmo, V., 1986, *Applied Optics*, 25, 565
- Hristov, V. *et al.* in preparation
- Hristov, V. *et al.* in preparation
- Hu, W., Sugiyama, N., Silk, J., 1997, *Nature* , 386, 37-43, astro-ph/9604166
- Kogut, A., and 19 colleagues 1993, *Ap. J.* , 419, 1

- Lee, A. T. *et al.* , 1999, in '3K Cosmology', AIP conference proceedings 476, pag. 224, Woodbury - New York, Maiani Melchiorri Vittorio Editors
- Masi, S., Aquilini, E., Cardoni, P., de Bernardis, P., Martinis, L., Scaramuzzi, F., Sforna. D., 1998, *Cryogenics*, 38, N.3
- Masi, S., Cardoni, P., de Bernardis, P., Piacentini, F., Raccanelli, A., Scaramuzzi, F., 1999, *Cryogenics*, 217-224, N.39
- Mather, J. C. *et al.* 1994, *Ap. J.* , 420, 439
- Mauskopf, P. *et al.* , 2000, *Ap. J. Lett.* 536, L59, astro-ph/9911444
- Mauskopf P. D., et al., *Applied Optics*, 36, 765, 1997
- Melchiorri, A. *et al.* , 2000, *Ap. J. Lett.* 536, L63, astro-ph/9911445
- Page, L.A., Cheng, E.S. & Myers, S.S., 1990, *Ap. J.* 335, L1
- Smoot, G. F., *et al.* 1991, *Ap. J. Lett.* , 371, L1
- Smoot, G., F., *et al.* 1992, *Ap. J.* 396, L1
- Tanaka, S. T., Clapp, A. C., Devlin, M. J., Figueiredo, N., Gundersen, J. O., Hanany, S., Hristov, V. V., Lange, A. E., Lim, M. A., *et al.* 1996, *Ap. J.* , 468, L81
- Ulich B.L. 1981, *AJ*, 86, 1619
- White, M., Scott, D. & Silk, J. 1994, *ARA&A*, 32, 319
- Wilbanks, T., Devlin, M., Lange, A. E., Sato, S., Beeman, J. W., and Haller, E. E. 1990, *IEEE Transactions on Nuclear Science*, 37, 566